



**HAL**  
open science

# Interhemispheric Asymmetry of the Equatorial Ionization Anomaly (EIA) on the African Sector Over 3 Years (2014-2016): Effects of Thermospheric Meridional Winds

A. Loutfi, F. Pitout, A. Bounhir, Z. Benkhaldoun, J. J. Makela, S. Abamni,  
K. Zyane, A. Elfakhiri

## ► To cite this version:

A. Loutfi, F. Pitout, A. Bounhir, Z. Benkhaldoun, J. J. Makela, et al.. Interhemispheric Asymmetry of the Equatorial Ionization Anomaly (EIA) on the African Sector Over 3 Years (2014-2016): Effects of Thermospheric Meridional Winds. *Journal of Geophysical Research Space Physics*, 2022, 127, 10.1029/2021JA029902 . insu-03867450

**HAL Id: insu-03867450**

**<https://insu.hal.science/insu-03867450>**

Submitted on 13 Apr 2023

**HAL** is a multi-disciplinary open access archive for the deposit and dissemination of scientific research documents, whether they are published or not. The documents may come from teaching and research institutions in France or abroad, or from public or private research centers.

L'archive ouverte pluridisciplinaire **HAL**, est destinée au dépôt et à la diffusion de documents scientifiques de niveau recherche, publiés ou non, émanant des établissements d'enseignement et de recherche français ou étrangers, des laboratoires publics ou privés.

Copyright

# JGR Space Physics

## RESEARCH ARTICLE

10.1029/2021JA029902

### Special Section:

Solar and Heliospheric Plasma Structures: Waves, Turbulence, and Dissipation

### Key Points:

- The Swarm measurements of ionospheric electron density over the African sector are presented for an extended period of 3 years
- By comparing the equatorial ionization anomaly (EIA) crests and the meridional winds, two types of responses are noticed for both quiet and disturbed conditions
- The relationship between the neutral wind and the strength of the EIA crest is quantified during both quiet and disturbed conditions

### Correspondence to:

A. Loutfi,  
loutfi.amal@gmail.com

### Citation:

Loutfi, A., Pitout, F., Bounhir, A., Benkhaldoun, Z., Makela, J. J., Abamni, S., et al. (2022). Interhemispheric asymmetry of the equatorial ionization anomaly (EIA) on the African sector over 3 years (2014–2016): Effects of thermospheric meridional winds. *Journal of Geophysical Research: Space Physics*, 127, e2021JA029902. <https://doi.org/10.1029/2021JA029902>

Received 26 AUG 2021  
Accepted 8 AUG 2022

## Interhemispheric Asymmetry of the Equatorial Ionization Anomaly (EIA) on the African Sector Over 3 Years (2014–2016): Effects of Thermospheric Meridional Winds

A. Loutfi<sup>1,2</sup> , F. Pitout<sup>2</sup> , A. Bounhir<sup>1,3</sup>, Z. Benkhaldoun<sup>1</sup>, J. J. Makela<sup>4</sup> , S. Abamni<sup>1</sup>, K. Zyane<sup>1</sup>, and A. Elfakhiri<sup>1</sup>

<sup>1</sup>Oukaimeden Observatory, Laboratory of High Energy Physics and Astrophysics, FSSM, Cadi Ayyad University, Marrakech, Morocco, <sup>2</sup>IRAP, CNES/CNRS/Toulouse University, Toulouse, France, <sup>3</sup>Faculty of Science, Mohammed V University, Rabat, Morocco, <sup>4</sup>Department of Electrical and Computer Engineering, University of Illinois Urbana-Champaign, Urbana, IL, USA

**Abstract** Observations made by the Langmuir probes on board the Swarm satellites and the Fabry–Perot interferometer installed at the Oukaimeden Observatory in Morocco have been systematically analyzed to study the effect of geomagnetic activity on the thermosphere–ionosphere system over 3 years. The annual variation of the electron density ( $N_e$ ) shows that during the day, the ionospheric density starts to increase at midlatitudes, with a single crest between 8 LT and 12 LT. It is also noticeable that the double crest structure is present between 12 LT and 00 LT: symmetric from 12 LT to 20 LT and asymmetric from 20 LT to 24 LT. Observations show strong seasonal variations, with  $N_e$  being lower around the June solstice. We have noticed the semiannual anomaly:  $N_e$  is higher around equinox than around solstice. For solstice seasons, the asymmetries in  $N_e$  are stronger at the December solstice than at the June solstice. For equinox seasons, we can notice equinoctial symmetry in all local time sectors, meaning that the same trend is observed for both equinoxes with or without symmetrical crests. The effect of meridional neutral winds on equatorial ionization anomaly (EIA) crests have been classified during both quiet and disturbed conditions. Over the studied region, the southward meridional winds have the tendency to enhance the northern crest of the EIA during quiet time and in a more pronounced way during geomagnetically disturbed conditions. Finally, we have quantified the relations between the thermospheric neutral winds data and the EIA by introducing an asymmetrical index.

## 1. Introduction

One of the important phenomena of the equatorial and midlatitude ionosphere is the equatorial ionization anomaly (EIA). It forms as a consequence of the equatorial fountain effect (Appleton, 1946; Martyn, 1947; MITRA, 1946; Schunk & Nagy, 2000), caused by the upward vertical  $E \times B/B^2$  plasma drift that elevates the  $F$  region ionosphere plasma to higher altitudes over the magnetic equator, followed by diffusion along the geomagnetic field lines, that moves the plasma down and away from the equator, forming ionization crests in both sides of the magnetic equator and an ionization trough over the dip equator. The latitudinal plasma distribution that characterizes the EIA (a trough at the magnetic equator and two crests at approximately  $\pm 17^\circ$  magnetic latitude) is well reproduced by many theoretical models (Anderson, 1973; Bailey & Balan, 1996; Bittencourt et al., 2007; Hanson & Moffett, 1966). This configuration can be significantly modified by several parameters. One of them is the thermospheric neutral wind.

Several studies have investigated the interhemispheric asymmetries of the midlatitude ionosphere, including the asymmetries of the latitudinal positions and densities of EIA crests. Moreover, the significant longitudinal variations of the EIA interhemispheric asymmetry have been studied in previous works (Lin et al., 2007; Luan et al., 2015; Tulasi Ram et al., 2009). Also, the seasonal variability of the interhemispheric asymmetry of the EIA crests with a global view in both solstices and equinoxes has been reported in the recent years (Balan et al., 2013; Lin et al., 2007; Luan et al., 2015; Tulasi Ram et al., 2009; Xiong & Lüher, 2013; Xiong et al., 2013). One of the prime candidates to govern the EIA variability is the change in magnitude and direction of the neutral wind field, which is produced by global or local pressure distributions and ambipolar diffusion linked with neutral density and scale height (Kelley, 2009; Sastri, 1990).

A superposition of annual, seasonal, and semiannual components, as well as the yearly average, can be used to represent yearly variations in the Earth's ionosphere. The semiannual cycle component has a 6-month period,

whereas the annual and seasonal cycles components have 12-month period. The annual component has the same phase in both hemispheres, whereas the seasonal components are 6 months out of phase in each hemisphere. Both the annual and seasonal components have their maxima and minima around the June and December solstices.

The temporal and spatial behavior of the ionospheric anomaly cannot be observed simultaneously with a single station due to the large longitudinal and latitudinal extent of the anomaly. Wu et al. (2004, 2008) studied ionospheric total electron content (TEC) in the Northern Hemispheric equatorial anomaly region from 1994 to 2003 with unprecedented spatial resolution, by analyzing dual-frequency GPS data collected from a meridional network of nine observational stations clustered around Taiwan (21.9°–26.2°N, 118.4°–121.6°E). They found that under low solar activity, the monthly values of  $I_c$  (magnitude of TEC at the northern anomaly crest) correlate well with the Dst geomagnetic activity index. They also revealed a weak semiannual variation in the northern EIA crest latitude—the winter and summer crests occurred at lower latitudes than the spring and autumn ones.

The seasonal, temporal, and longitudinal variations in EIA asymmetry also depend on the displacement of the geographic and geomagnetic equators and on the magnetic declination angle (Dang et al., 2016; Luan et al., 2015; Tulasi Ram et al., 2009). In the African sector, there are few studies about the EIA. Bosco et al. (2016) studied the variability of the EIA, they focus on the analysis of the crest-to-trough TEC ratio (TEC-CTR) but only in the southern crest region during the high solar activity year 2012. Bolaji et al. (2017) reported the roles of equatorial electrojet (EEJ) and integrated equatorial electrojet (IEEJ) in controlling EIA morphology using the TEC from 22 GPS receivers and three ground-based magnetometers (Magnetic Data Acquisition System, MAGDAS) over Africa and the Middle East during the quietest periods. However, on some of the quietest days, they suggested that the EIA morphology could be controlled by the thermospheric meridional neutral winds, unfortunately not being able to verify it due to the lack of wind measurements over Africa and Middle East in 2009. There is also a similar study aiming at characterizing the EIA in the East African region but only for 1 year (2012; Kassa et al., 2014).

The effect of the meridional wind on asymmetry generation has been explained in several studies by the plasma recombination. For instance, if the meridional neutral wind is blowing north to south (south to north), it will drive plasma a little bit up in ionospheric height where less recombination of ions occurs, leading to larger plasma density in the Northern (Southern) Hemisphere than that in the southern (northern) one. In this work, a discussion is led to see whether the plasma recombination can explain all the cases of interhemispheric asymmetry of the topside ionosphere. Thus, the interhemispheric asymmetry of the topside ionosphere needs to be further investigated and especially in the African sector where the ground-based data are limited. In this study, we take advantage of the Swarm mission to conduct coordinated ground- and space-based observations, in which the broad context provided by Swarm is augmented by location-specific information from Fabry–Perot interferometer (FPI) in the area.

Studying the coupling between the ionosphere and thermosphere has recently become more feasible, with the increasing availability of observations. In the past decade, there have been a large number of observational and modeling studies of the coupling processes between those regions, including waves and dynamics and their impact in the coupling. However, many key challenges and issues remain open, as there are large discrepancies in estimates of some of these processes. In this work, we study the coupling of the ionosphere–thermosphere system during both quiet and disturbed periods, through studying the effect of meridional winds on the EIA crests asymmetry. We adopted the electron density measurements from space instruments and the neutral wind measurements over the African sector from a ground-based instrument. Data used in this study were collected during the declining solar cycle (2014–2016). In Section 2, we describe the FPI instrument and methods used to produce the estimates of the thermospheric neutral winds. Section 3 provides annual and seasonal variations of ionosphere electron density in the magnetic meridian lines above the Oukaimeden Observatory during 3 years of observations. We also produce a general classification of the thermospheric–ionospheric response to the storms observed during the study period. Then, we present an analysis of the disturbed data that has been achieved to quantify the effects of the geomagnetic storm phase on meridional winds and vertical electron density responses over Oukaimeden Observatory. Finally, the last section is devoted to conclusions.

## 2. Data and Method

### 2.1. Fabry–Perot Interferometer

The thermospheric wind data are provided by a FPI installed at Oukaimeden Observatory in Morocco (31.206°N, 7.866°W; 22.84°N magnetic; elevation: 2,700 m) and described in detail in Makela et al. (2009), Kaab et al. (2017), and Malki et al. (2018). The FPI (Harding et al., 2014; Makela et al., 2011) measures the thermospheric wind and temperature by observing the 630-nm airglow generated by the excitation of  $O^{1D}$  arising from the dissociative recombination of  $O_2^+$ , which takes place at an average altitude of approximately 250 km. Kaab et al. (2017) modeled the 630.0 nm emission peak altitude over Oukaimeden Observatory as a function of local time and day of year. This instrument contains (a) a sky scanner system having two mirrors with dual-axis that can be moved to point any direction, (b) a narrow band interference filter to isolate the emission of interest, (c) a 42 mm diameter etalon with an air gap spacing of 15 mm, and finally (d) a thermoelectrically cooled CCD to capture the interference pattern produced by the etalon. The resultant interference pattern is analyzed using the methodology described in detail in Harding et al. (2014). Individual exposure times for each observation are a function of the brightness of the emission and typically range from 30 s to 10 min. Observations are typically made in a cardinal observing mode (zenith, east, north, west, and south), with an additional observation made of a frequency stabilized laser from which the FPI's instrument function is deduced.

We adopt the method detailed in Fisher et al. (2015) and Kaab et al. (2017) to study thermospheric wind variability. We sort and bin the filtered data into 15-min intervals, for each interval, we calculate a weighted average,  $v_m$ , such that

$$v_m = \frac{\sum_i^N v_i \cdot w_i}{\sum_i^N w_i} \quad (1)$$

where  $v_i$ ,  $w_i = \frac{1}{\sigma_i^2}$ , and  $N$  are respectively the value of the wind (meridional), its weight (the inverse of its uncertainty,  $\sigma_i$ , squared), and the number of measurements in the given bin. The meridional measurements taken while looking north and south are separated by 500 km. Despite this separation, we calculate the meridional components of thermospheric winds from the average of the north and south measurements to obtain the meridional wind estimates.

For this study, 545 nights with FPI data available from 2014 to 2016 were classified according to two geomagnetic indices, SYM-H and Kp. We have 504 quiet nights referring to SYM-H  $\geq -20$  and Kp  $\leq 2$ , and 41 disturbed nights with SYM-H  $\leq -50$  and Kp  $\geq 5$ . This classification (quiet and disturbed days) will be presented for determining the ionosphere–thermosphere coupling.

Figure 1 shows the change in global SYM-H (top), Kp-index (middle), and F10.7 (lower) over 3 years from 2014 to 2016. This period is characterized by two major geomagnetic storms (SYM-H  $< -200$  nT and Kp  $\geq 7$ ), which are extreme events of space weather in the current 24th solar cycle. The variation in F10.7 index indicates a decrease in solar activity, this period coincided with the declining phase of solar cycle 24, which peaked in 2014.

### 2.2. Swarm

Swarm is a European Space Agency mission designed to study the Earth's magnetic field (Friis-Christensen et al., 2008). It is a constellation of three satellites equipped with identical instruments and placed in polar orbits (inclination 87.55°). The payload is designed to measure the magnetic field, as well as the features that can locally modify it. Swarm A and C are located at 460 km altitude whereas Swarm B is flying at 530 km. Langmuir Probes (LPs) on board Swarm satellites allow for estimates of the electron density ( $N_e$ ) and temperature ( $T_e$ ) of the ambient plasma. In the next section, we will analyze the variation of the electron density as a function of magnetic latitude and in different local time (LT) sectors. Most of the processes occurring in the ionosphere have a marked magnetic latitudinal dependence (Davies, 1990; Kelley, 2009). Thus, we converted geographical coordinates into quasi-dipole coordinates (Emmert et al., 2010). The latitudinal resolution of the averaged plasma density is 1°. Midlatitudes represent the region where the magnetic latitudes are between 30° and 60°, whereas, low latitudes represent the region where the magnetic latitudes are below 30°. Swarm Alpha (A), Swarm Bravo (B), and Swarm Charlie (C) satellites are named hereafter SWA, SWB, and SWC, respectively. For creating climatologies of the

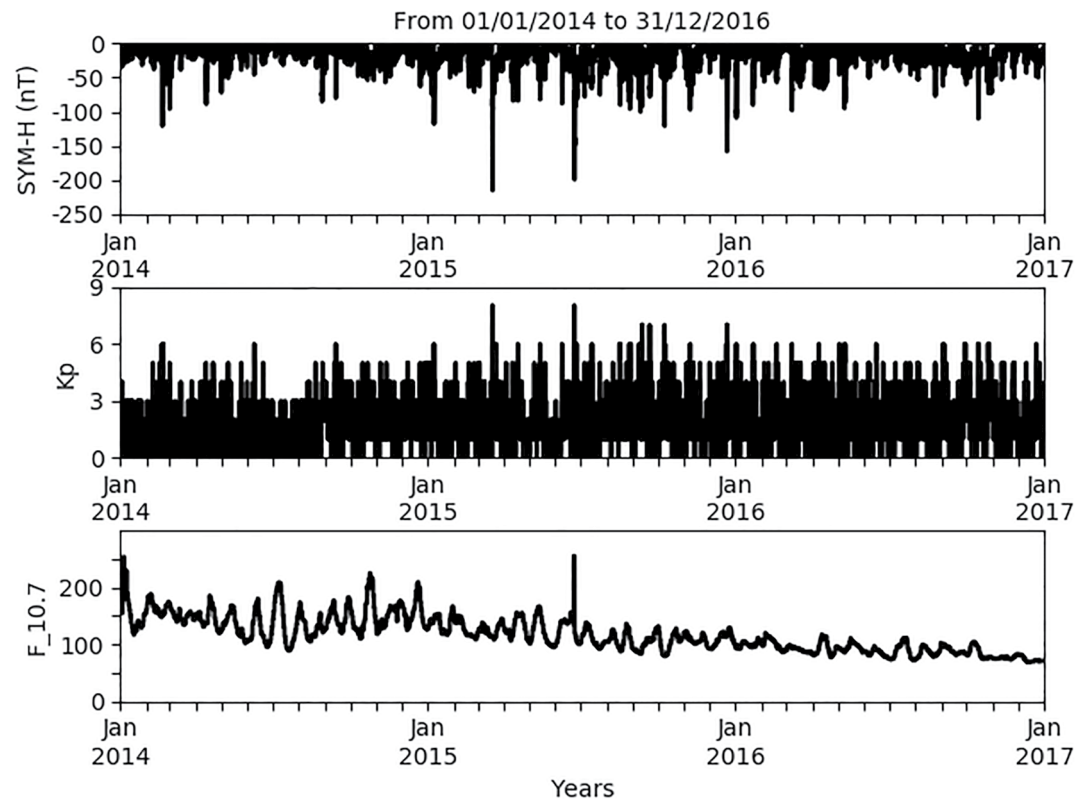


**Figure 1.** Variation of global SYM-H (top), Kp-index (middle), and F10.7 (lower) over 3 years from 2014 to 2016.

ionosphere electron density, we have selected all Swarm satellite passes that cross a rectangle of  $-60^{\circ}\text{S}$ ,  $60^{\circ}\text{N}$  in magnetic latitude and  $-7.88^{\circ}-4^{\circ}\text{W}$  and  $-7.88^{\circ}+4^{\circ}\text{W}$  in geographic longitude. Figures 2 and 3 are created in an Earth-fixed reference frame with magnetic latitudes ranging from  $60^{\circ}\text{S}$  to  $60^{\circ}\text{N}$ .

### 2.3. The Horizontal Wind Model

The EIA is characterized by a trough at the magnetic equator and two crests at approximately  $\pm 17^{\circ}$  magnetic latitude, as reported in the literature. This latitudinal plasma distribution is affected by several parameters, one of these parameters is the meridional wind. The explanation of the effect of the meridional wind on the EIA interhemispheric asymmetry along the magnetic meridian on the Africa sector requires determining the direction of the meridional winds on a nonlocal scale; this means we need to know whether the meridional winds are (a) transequatorial (blowing from North to South or from South to North), (b) convergent (blowing toward the equator in both hemispheres), and (c) divergent (blowing toward the poles in both hemispheres). Horizontal Wind Model (HWM) provides a statistical representation of the expected neutral winds for a given location and time based on prior measurements and is used in this study to provide estimates of the winds where measurements are not available (Drob et al., 2015). This model describes the atmosphere's vector wind fields from the surface up to the exobase ( $\sim 450$  km) by the estimate of the meridional and zonal components of the wind as a function of latitude, longitude, altitude, day of the year, and time of day for quiet and geomagnetic conditions through a 3-hr ap index. HWM model has two components (quiet time HWM14 + disturbance wind model DMW07 [Emmert et al., 2008]).

To have a more accurate comparison of the FPI data set with the model and compose the missing data in the Southern Hemisphere in the same magnetic meridian and near to the southern EIA crest, we have run the model at each of the four points where the FPI line of sight intersects with the altitude 250 km. Then, the modeled average meridional and zonal winds have been estimated following the same procedure as with the measured FPI data (see Section 2.1).

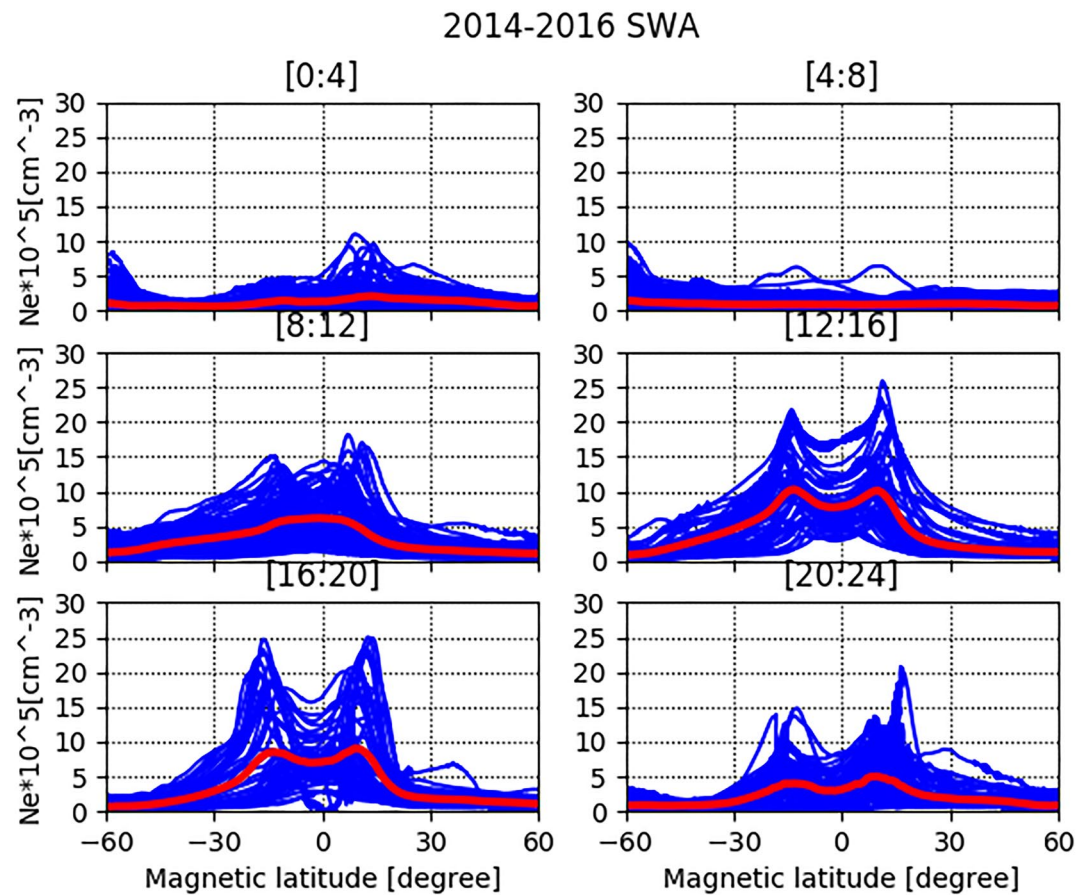


**Figure 2.** Latitudinal distribution of electron density around 7.866°W magnetic meridian sector ( $\pm 4^\circ$  intervals) in different local time sectors. Each panel shows all SWA passages observations within the 4-hr interval (blue lines) and their average (red line) over 3 years of the whole selected data set.

### 3. Results and Discussion

#### 3.1. Latitudinal Distribution Average of Ionospheric Electron Density

As an example of the method used throughout the paper, Figure 2 presents in blue the electron density measured on board SWA during all the passes in the area described in the previous section. The mean variation of the ionospheric plasma density is shown in red. The passes are sorted only by local time (six panels for six local time sectors). The panels thus mix different seasons and levels of geomagnetic activity.

Figure 3 presents the latitudinal distribution of the ionospheric electron density at around 7.866°W magnetic sector ( $\pm 4^\circ$  longitude intervals) at different local time sectors for all data sets available over 3 years (2014–2016). From Figure 3, we can notice that in the day and at night, the density is always very low at midlatitudes (not exceeding  $2.0 \times 10^5 \text{ cm}^{-3}$ ), at all satellites. During nighttime, from midnight to 8 LT: it is at its lowest values even at midlatitudes (varying between  $0.5 \times 10^5$  and  $2.0 \times 10^5 \text{ cm}^{-3}$ ). Yonezawa (1971) show that, in general, the relative amplitude of the NmF2 annual component decreases slowly with increasing latitude during daytime and is smaller at nighttime compared to daytime. Bailey et al. (2000) investigated the topside ionosphere using observations made by the Hinotori satellite at 600 km. They reported from yearly variations of the topside ionosphere at low latitudes, lower electron densities during nighttime than daytime. During the day, the ionospheric density starts to increase at midlatitudes, with a single crest, not centered at the magnetic equator but located at 3°S, between 8 LT and 12 LT. In this time frame, the peak density is about  $6.0 \times 10^5 \text{ cm}^{-3}$  for SWA and SWC and  $4.0 \times 10^5 \text{ cm}^{-3}$  for SWB. For more details concerning the density at the peak and its magnetic latitude, see Table 1. Fathy and Ghamry (2017) reported that the majority of single crests (86%) is observed between 08:00 and 12:00 magnetic local time. They reported that the lowest number of single crests (14%) is observed within

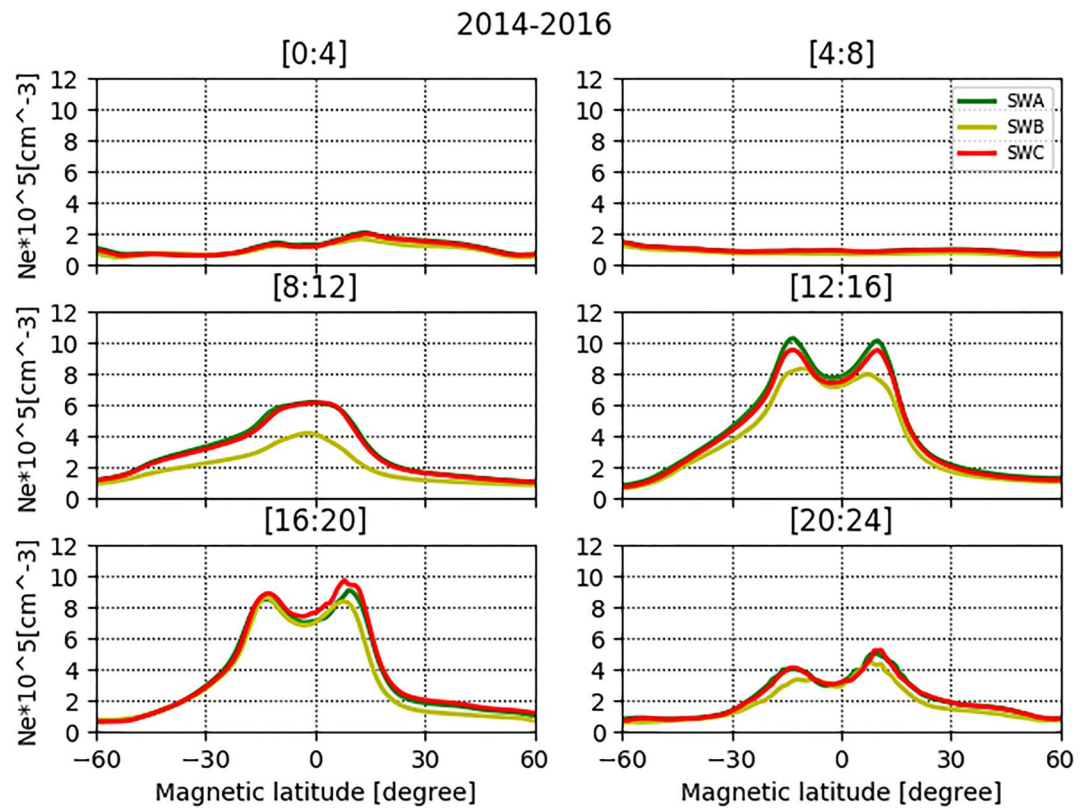


**Figure 3.** Same as Figure 2. Only the 3-year averages of SWA (green line), SWB (yellow line), and SWC (red line) are shown.

the dawn side and before midnight. It is also noticeable that the EIA crest structures are present between 12 LT and midnight for SWA, SWB, and SWC: symmetric from noon to 20 LT and asymmetric from 20 LT to 24 LT. The peaks are located on average at  $-13^\circ$  and  $10^\circ$  North and the trough (minimum electron density between the peaks) is located at  $-3^\circ$  North. More information about the electron density of the northern crest, the southern crest, and the trough of the EIA and their magnetic latitudinal position is provided in Table 2. Table A4 includes the number of satellite passes taken for the analysis.

It is interesting to see how the measured electron density at the three satellites can be very close or different. For instance, SWB measures lower values of the electron density than SWA and SWC between 8 LT and 16 LT; this is consistent given the fact that it is located at a higher altitude. Balan et al. (2013), by using SUPIM model, reported that in the bottom side ionosphere (e.g., 200 km), there is no significant asymmetry in  $N_e$ . Their simulation results show that the asymmetry in  $N_e$  only exists at altitudes near and above the ionospheric peak, especially in the topside ionosphere (e.g., 400 km). However, between 16 LT and 20 LT, in the Southern Hemisphere, all Swarm measurements coincide, which is not the case for the Northern Hemisphere. The existent asymmetry in the Earth's magnetic field could be the first candidate behind most of the ionospheric electron density hemispheric asymmetries observed in this present work for both annual and seasonal trends. To substantiate our argument

in this regard, we have run the International Geomagnetic Reference Field (IGRF-12; Thébault et al., 2015) model to show the latitudinal distribution of the total magnetic field intensity around  $7.866^\circ\text{W}$  magnetic meridian sector from 2014 to 2016 as shown in Figure 4. In the Northern Hemisphere, the total magnetic field intensity is stronger than in the Southern Hemisphere. Forster and Cnossen (2013) found that the asymmetry of the magnetic field, both in strength and orientation, creates substantial hemispheric differences in the neutral wind and plasma drift in the high-latitude upper atmosphere. Barlier et al. (1974) showed that the north-south asymmetries observed in the thermospheric data like temperature, density, concentration, and winds

**Table 1**  
Details on the Electron Density and the Magnetic Latitude of the Single Crest Corresponding to Figure 3

Sector LT	[8:12]		
Satellite	A	B	C
$N_e$ (single crest) ( $10^5 \text{ cm}^{-3}$ )	6.18	4.19	6.14
Mlat (single crest) ( $^\circ$ )	-1	-2	0

**Table 2**  
Details on the Electron Density and the Magnetic Latitude of the Northern Crest (NC), Southern Crest (SC), and the Trough Corresponding to Figure 3

Sector LT	[0:4]		
Satellites	A	B	C
$N_e$ (NC) ( $10^5 \text{ cm}^{-3}$ )	2.1	1.69	2.01
Mlat (NC) ( $^\circ$ )	13	13	14
$N_e$ (SC) ( $10^5 \text{ cm}^{-3}$ )	1.45	1.26	1.36
Mlat ( $^\circ$ )	-11	-10	-10
$N_e$ (trough) ( $10^5 \text{ cm}^{-3}$ )	1.29	1.16	1.18
Mlat (trough) ( $^\circ$ )	-6	-1	-4
Sector LT	[12:16]		
$N_e$ (NC) ( $10^5 \text{ cm}^{-3}$ )	10.13	7.98	9.52
Mlat (NC) ( $^\circ$ )	10	7	10
$N_e$ (SC) ( $10^5 \text{ cm}^{-3}$ )	10.27	8.34	9.53
Mlat ( $^\circ$ )	-13	-10	-13
$N_e$ (trough) ( $10^5 \text{ cm}^{-3}$ )	7.74	7.16	7.42
Mlat (trough) ( $^\circ$ )	-3	-2	-3
Sector LT	[16:20]		
$N_e$ (NC) ( $10^5 \text{ cm}^{-3}$ )	9.07	8.36	9.73
Mlat (NC) ( $^\circ$ )	9	8	8
$N_e$ (SC) ( $10^5 \text{ cm}^{-3}$ )	8.52	8.61	8.89
Mlat ( $^\circ$ )	-14	-14	-13
$N_e$ (trough) ( $10^5 \text{ cm}^{-3}$ )	7.01	6.85	7.42
Mlat (trough) ( $^\circ$ )	-3	-3	-3
Sector LT	[20:24]		
$N_e$ (NC) ( $10^5 \text{ cm}^{-3}$ )	5.01	4.49	5.24
Mlat (NC) ( $^\circ$ )	10	8	11
$N_e$ (SC) ( $10^5 \text{ cm}^{-3}$ )	4.03	3.37	4.13
Mlat ( $^\circ$ )	-13	-7	-13
$N_e$ (trough) ( $10^5 \text{ cm}^{-3}$ )	2.96	2.9	3.07
Mlat (trough) ( $^\circ$ )	-2	-1	-2

result from geomagnetic field asymmetry. If thermospheric neutral particles are affected by the existent asymmetry in the Earth's magnetic field, ionized ones should be even more directly affected. Furthermore, the thermosphere being the primary driver of the ionosphere, they behave in tandem.

The average latitudinal distribution of electron density in different local time sectors over 3 years may hide important information and to gain more insight, the next paragraph is dedicated to the seasonal variability.

### 3.2. Seasonal Variability of Ionospheric Electron Density

Figures 5–7 show seasonal variability of the time evolution of the ionospheric plasma density structure at the midlatitude and low-latitude regions at around 7.866°W magnetic meridian sector ( $\pm 4^\circ$  longitude intervals) of all data available for different local time sector over 3 years (2014–2016). At first glance to Figures 5–7, we can see that the ionospheric density is very low at night and the lowest for the June solstice at other local times. We can also see a hemispheric asymmetry in the evolution of the electron density where it decreases slowly with latitude in the Southern Hemisphere whereas the opposite is observed in the northern one. This asymmetry could find its origin, partly at least, in the asymmetry of the magnetic field itself. In this context, Laundal et al. (2017) mapped the geomagnetic field over the globe and found significant differences between conjugate points and correlated them to the asymmetry of the geomagnetic field. They showed that those differences can lead to asymmetries in thermospheric winds, ionospheric convection, currents and magnetic field perturbations, electron density, ion outflow, and auroral emissions. They reported that the asymmetries between the geomagnetic field in the Northern and Southern Hemispheres introduce an asymmetry in the solar EUV radiation absorption and in the neutral composition, leading to hemispheric differences in the *F* region electron density. North–South asymmetry in the magnetic field, together with the offset between the magnetic and geographic poles, variations in the Sun–Earth distance, result in the Southern Hemisphere high-latitude ionosphere experiencing greater exposure to EUV radiation compared to the Southern Hemisphere. Additionally, energy inputs at high latitudes and changes in the (horizontal and vertical) transport modifies  $[O/N_2]$ . As the energy input, in general and during geomagnetic storms in particular, is related to the geomagnetic field geometry, the thermosphere composition, and its impact on production and loss of ions and electrons, will be impacted by hemispheric asymmetries in the geomagnetic field. So **several** of these differences are not yet fully understood and should be a topic of research for years to come.

From 8 LT to 12 LT, the ionospheric density has a single crest morphology with September equinox highest values for SWA and SWC. This result is consistent with the empirical model outputs from 9 LT to 12 LT of seasonal variations of equatorial *F* region quiet time vertical plasma drifts at an altitude of about 600 km using ion drift observations on board the ROCSAT-1 from March 1999 to July 2004 (Fejer et al., 2008). From 12 LT to 16 LT, the March equinox density becomes the highest one. This feature is also in a good agreement with the seasonal variations of vertical plasma drifts reported by Fejer et al. (2008) from 13 LT to 16 LT. From 16 LT to 20 LT, for SWA and SWC, the December solstice density becomes the highest except in equatorial and northern midlatitudes regions. It is very interesting to see that at this local time, even if SWB is located at a higher altitude, its March density is the highest by 50% in comparison with SWA and SWC density. This observation could be related to enhanced vertical plasma drift (Lin et al., 2007) and/or a supposed existence of a second ionospheric layer occurring in Springtime at higher altitudes (Balan & Bailey, 1995). The values of the ionospheric density peaks (single or double) are given in Tables A1–A3 along with their magnetic latitude and that of the trough. Table A5 includes the number of satellite passes taken for the analysis.

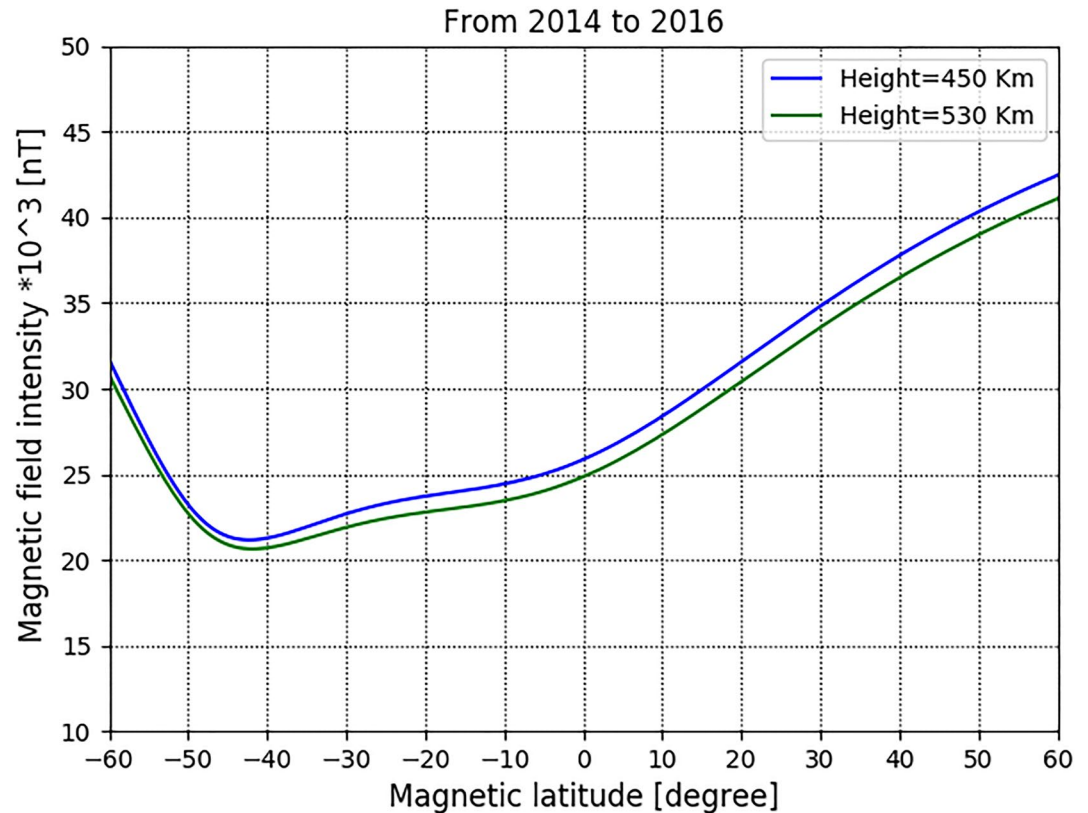


**Figure 4.** Latitudinal distribution of the total magnetic field intensity around 7.866°W magnetic meridian sector over 3 years.

For solstice seasons, the average  $N_e$  values indicate the existence of two different EIA asymmetries:  $N_e$  is higher in the Northern (Southern) Hemisphere than in the southern (northern) one in the December solstice (June solstice). We also note that the asymmetries in the  $N_e$  are stronger at the December solstice than at the June solstice. This feature found by the Swarm satellites observation of electron density is in good accordance with the result illustrated by Titheridge and Buonsanto (1983). They reported that the TEC measured at conjugate sites at  $\pm 20^\circ$  latitude and nonconjugate sites near  $\pm 35^\circ$  is large in December solstice than in June solstice in both the Southern and Northern Hemispheres. Besides, Su et al. (1998), by using the observation of electron density made by the Hinotori satellite at the Kagoshima Space Centre (KSC, 131°E), found that the amplitude of the EIA crests asymmetry to the magnetic equator is smaller at the June solstice than at the December one. Kalita et al. (2022) studied the EIA anomaly using ionosondes in two pairs of conjugate stations along the  $100^\circ\text{E} \pm 5^\circ\text{E}$  meridian. They found that during June/July, the morning time hemispheric asymmetry is larger on the winter side, temporarily reduces in the midday period, and then reverses sign (larger in summer side) in the afternoon. This is contrasting with our result, where during June solstice the asymmetry does not reverse sign with local time and is always higher in the summer side hemisphere. These asymmetries of solstice seasons amplitude of the EIA crests are partially explained by the solar flux difference in two solstices due to the change in Sun–Earth distance suggest by Su et al. (1998). Furthermore, several studies suggest that the transequatorial neutral wind from summer to winter hemisphere can be the primary reason for the EIA crests asymmetry in solstice seasons (e.g., Dang et al., 2016; Hanson & Moffett, 1966; Lin et al., 2007; Luan et al., 2015). Loutfi et al. (2020) have reported transequatorial neutral winds above the Oukaimeden Observatory from summer to winter. Solstice seasons, characterized by the winter anomaly, have been explained successfully by changes in thermospheric composition, the atomic/molecular ratio in winter is higher than in summer (e.g., Rishbeth & Setty, 1961; Rüster & King, 1973), and from global thermospheric circulation (e.g., Millward et al., 1996).

For equinox seasons, we can notice equinoctial symmetry at all local time sectors. meaning that the same trend is observed for both equinoxes with or without symmetrical crests. These features of the equinoctial symmetry are in good accordance with the result reported by Bailey et al. (2000). EIA crests asymmetry is observed from

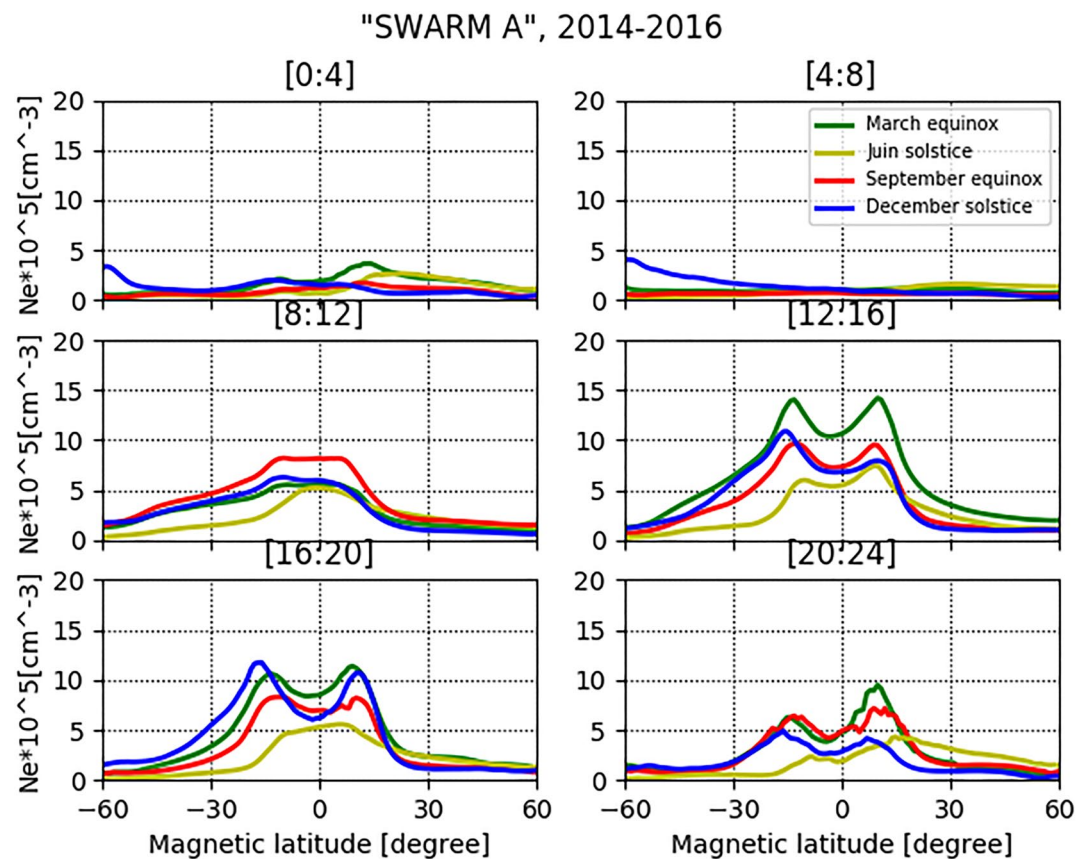


**Figure 5.** The seasonal variation of the ionospheric plasma density structure at the midlatitude and low-latitude regions at around 7.866°W magnetic meridian sector ( $\pm 4^\circ$  longitude intervals) in different local time sectors for SWA.

20 LT to 04 LT where the Northern Hemisphere crest density is higher than the southern one. The average of the electron density in March equinox is greater than the September one except from 8 LT to 12 LT, whereas the opposite is observed for the single crest ionospheric density. Chen et al. (2017), by using ion density ( $N_f$ ) data from ROCSAT-1, reported that the EIA crests asymmetry observed mainly between 16 LT and 24 LT in March equinox for longitude sectors ( $0^\circ$ – $60^\circ$ W) is higher in the Northern Hemisphere than the southern one. We have observed the same trend. They also reported by analyzing the ( $120^\circ$ – $180^\circ$ W) in longitude sectors, that in this case the opposite trend is observed: the EIA crest asymmetry is higher in the **Southern Hemisphere** than the northern one. They explained that the zonal winds are the reason for this longitudinal asymmetry. Kalita et al. (2022) reported that the anomaly at the conjugate stations is highly asymmetric even during the equinoctial months of March and October, whereas it is nearly symmetric during April. Lin et al. (2007), by using ROCSAT and DMSP satellites, reported seasonal variations of local time-averaged vertical plasma drifts at different longitude sectors. In the longitude sector ( $\sim 310^\circ$ – $360^\circ$ ), which includes the area of interest in our paper, from 12 LT to 20 LT, they reported that the vertical drift in spring equinox is the highest, followed by the December solstice one and then the autumn equinox one, and finally the June solstice one. This result correlates with our observed variation of the ionospheric electron density. A twist in the drift from 20 LT to 24 LT has been observed by Lin et al. (2007), with the June solstice drift was the largest, while the other season drifts were relatively close to each other. This result also correlates with ours in the Northern Hemisphere, where the June solstice density became the highest and decreases slowly with latitude. In the American sector, between 20 LT and 24 LT, they reported the highest vertical drift for the December solstice. One may conclude that in this sector, the December solstice electron density is the highest in the Northern Hemisphere with opposite observation in the Southern Hemisphere. This longitudinal dependence of the EIA crests is poorly understood. It constitutes one of the primary goals of the ICON satellite (Immel et al., 2018), which aims to explore the interconnection between the Earth weather and the space's one. The transequatorial wind is a good candidate explaining the highest electron density in the Northern

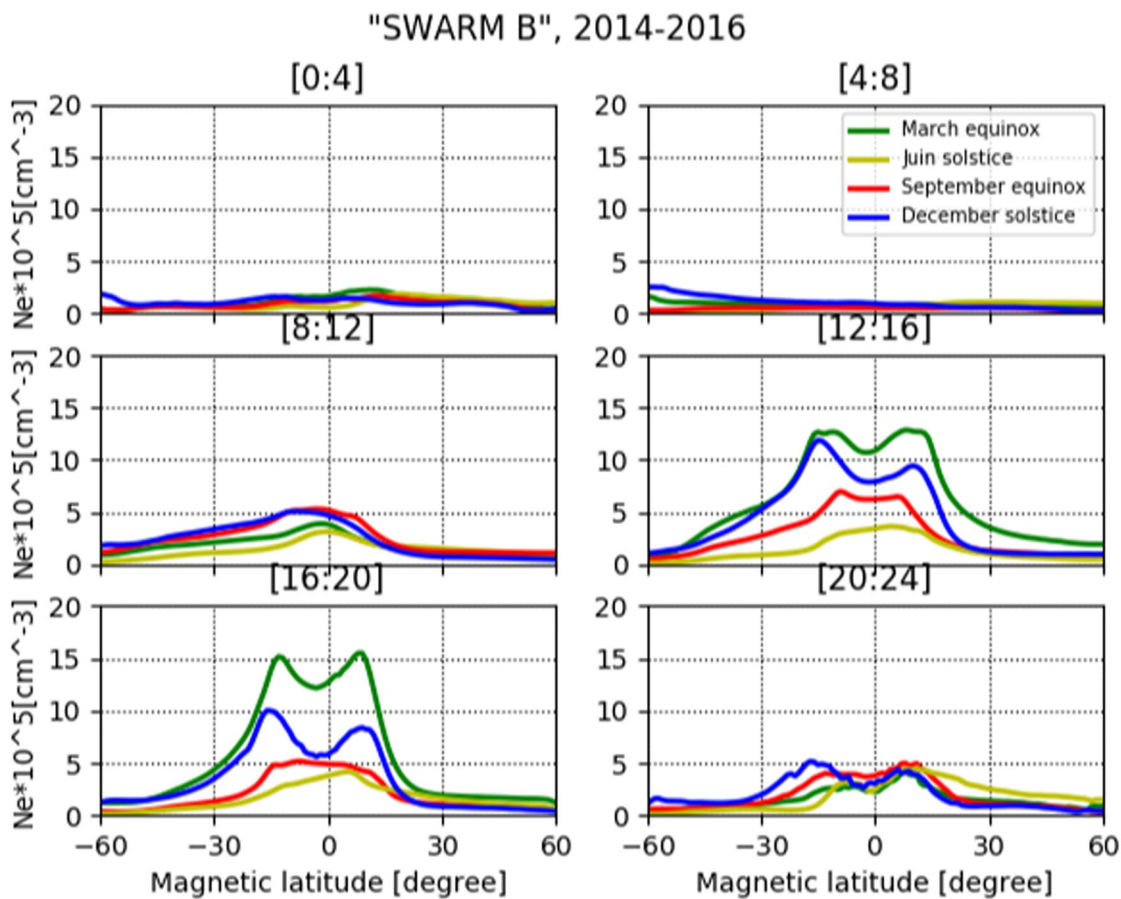


Figure 6. Same as Figure 5, but for SWC.

(Southern) Hemisphere during December solstice (June solstice); it blows from the summer hemisphere to the winter hemisphere, which pushes the plasma equatorward and poleward along the field line (referred to as pile-up effects [Wan et al., 2022]) in the summer and winter hemispheres, respectively. These neutral wind effects contradict/favor the ambipolar diffusion in the summer/winter hemisphere; hence, the development of EIA crest in the summer/winter hemisphere is inhibited/promoted, resulting in that the time points of EIA's development show clear winter hemispheric priority. On the other hand, the symmetric EIA crests in the rest of the local time sectors (12–16 LT) in equinox seasons can be explained by the symmetry of both the solar photoionization and the thermospheric parameters in two hemispheres in this time frame. A mechanism for the equinoctial asymmetry has been studied using CTIP (Coupled Thermosphere Ionosphere Plasmasphere model). The model results reproduce the observed equinoctial asymmetry and suggest that the asymmetries are caused by the north-south imbalance of the thermosphere and ionosphere due to the slow response of the thermosphere arising from the effects of the global thermospheric circulation (Bailey et al., 2000).

From comparing the average electron density of the equinox and solstice seasons, we have noticed the semiannual anomaly: the electron density is higher at the equinoxes than at the solstices. This is in accordance with the observations made by the Hinotori satellite (Bailey et al., 2000). The reason for this feature is not well understood. Fuller-Rowell (1998) suggested that the source of the semiannual anomaly is the thermospheric spoon: the general thermospheric circulation reduces the atomic oxygen density, therefore, raises the molecular nitrogen and oxygen densities at solstices compared to equinoxes.

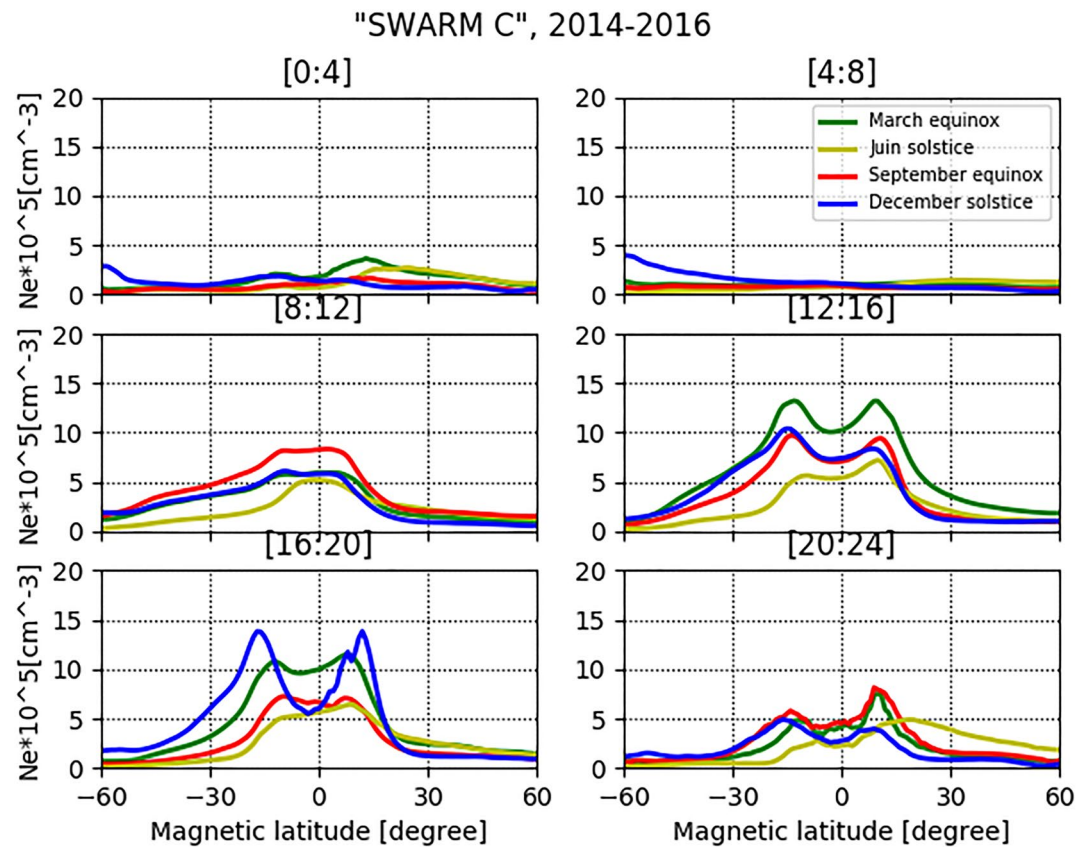


Figure 7. Same as Figure 5, but for SWB.

### 3.3. Coupled Ionosphere–Thermosphere System

#### 3.3.1. A Few Typical Examples

The thermospheric neutral wind especially the meridional component has a very important effect in the final configuration of the EIA. By analyzing the data observed from Swarm satellites (electron density) and the meridional wind obtained by the FPI in the Northern Hemisphere, we aim to explore the ionosphere–thermosphere coupling system during both quiet and disturbed nights over 3 years (2014–2016). Forty-one storms with  $\text{SYM-H} \leq -50$  nT,  $K_p \geq 5$  have been recorded during the period of study. From observed results, most ionospheric electron densities provided by Swarm during geomagnetically disturbed conditions are much lower than correspondent quiet time. The HWM14 model has been used to provide a broader estimate of the geographic distribution of the meridional winds. We introduce an asymmetry index  $a$ , which is the difference between the largest EIA crest electron density values at the Northern Hemisphere  $(Ne)_{nc}$  and the southern one  $(Ne)_{sc}$  divided by their average, according to Equation 2. For determining the EIA crests, we have taken the maximum density in the Northern (Southern) Hemisphere where the magnetic latitude greater than  $+7^\circ$  (smaller than  $-7^\circ$ ):

$$a = \frac{2 * [(Ne)_{nc} - (Ne)_{sc}]}{(Ne)_{nc} + (Ne)_{sc}} \quad (2)$$

A positive (negative)  $a$  index means an asymmetry with higher  $N_e$  in the Northern (Southern) Hemisphere. We selected the bands extending from  $60^\circ\text{S}$  to  $60^\circ\text{N}$  magnetic latitude covering midlatitude and low-latitude regions. Figure 8 provides four examples of the electron density behavior during quiet nights (four top panels) and disturbed ones (four bottom panels). All left panels show the electron density recorded by the LP on board a Swarm spacecraft. All right panels show the corresponding meridional wind speed given by the HWM14 model with a dot representing the FPI measurement at Oukaimeden (positive values are northward meridional winds). This figure includes the predictions of the HWM14 model from  $60^\circ\text{S}$  to  $60^\circ\text{N}$ , from which one can conclude the

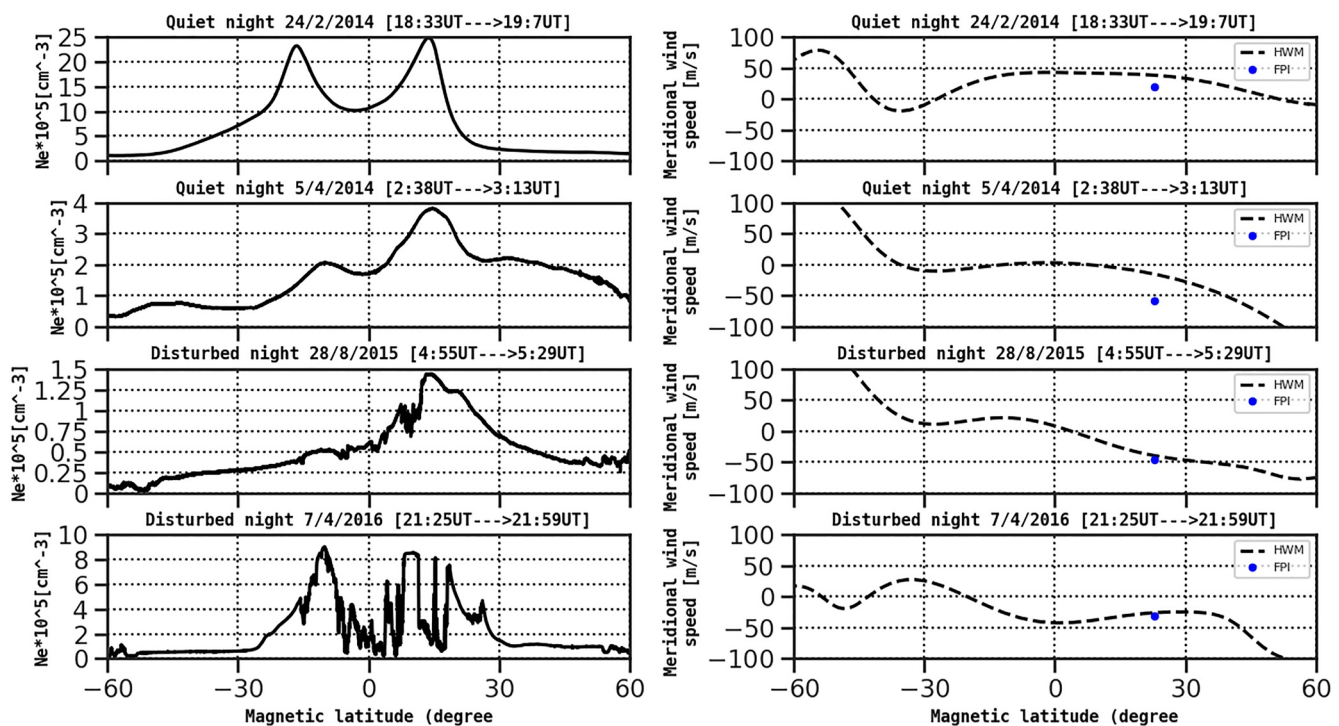


**Figure 8.** Four examples of the electron density behavior during quiet nights (four top panels) and disturbed ones (four bottom panels). All left panels show the electron density recorded by the Langmuir probe on board a Swarm spacecraft. All right panels show the corresponding meridional wind speed given by the HWM14 model with a dot representing the Fabry–Perot interferometer (FPI) measurement at Oukaimeden (positive values are northward meridional winds).

existence or absence of transequatorial winds. Two typical types of EIA crests response are shown in the present section: (a) asymmetrical EIA crests and (b) symmetrical EIA crests with respect to the equator. Both cases are observed during both quiet and disturbed conditions. From our observations, the case of symmetrical EIA crests most likely is generated by either weak wind speeds or by converging/diverging winds with about the same velocity in both hemispheres (as estimated by HWM and confirmed in the Northern Hemisphere using FPI data).

In fact, in the top panels of Figure 4 representing data of 24 February 2014 quiet night, the EIA crests are symmetrical and the FPI meridional wind at Oukaimeden is northward. The HWM predicts poleward meridional winds (divergent) in both hemispheres at low- and midlatitude. Concerning the bottom panels representing data of 7 April 2016 disturbed night, the EIA crests are more or less symmetrical with convergent meridional winds that are equatorward in both hemispheres according to HWM predictions. In this night, given the location (equatorial and low latitude) and the time (after sunset from 21:25 UT to 21:51 UT), the fluctuations of electron density observed are plasma bubbles. Plasma bubbles are known to be generated at equatorial regions through the nonlinear evolution of the Rayleigh–Taylor Instability as the prereversal enhancement of the vertical plasma drift in the postsunset sector (Fejer et al., 2008) lifts the equatorial *F* layer. **Plasma bubbles drift in the zonal direction and get mapped in the meridional direction (other latitudes)**. Oliveira et al. (2020) reported that the plasma bubbles rise to the topside of the ionosphere in a buoyant motion. As the structures rise above the geomagnetic equator, they spread to other latitudes, due to their field alignment.

Moreover, this configuration of symmetry and asymmetry of the EIA crests during these two nights is roughly consistent with our seasonal variation reported in Section 1. On the other hand, a northward or southward transequatorial meridional wind is a good candidate for this EIA asymmetry generation. This fact is illustrated in the data of 5 April 2014 quiet night and 28 August 2015 disturbed night where EIA crests asymmetry is observed along with transequatorial winds blowing from Northern to Southern Hemisphere according to FPI data and HWM predictions. We specify that the northern crest is denser than the southern one. From observed results, most ionospheric electron densities provided by Swarm during geomagnetically disturbed conditions are much lower than correspondent quiet time.

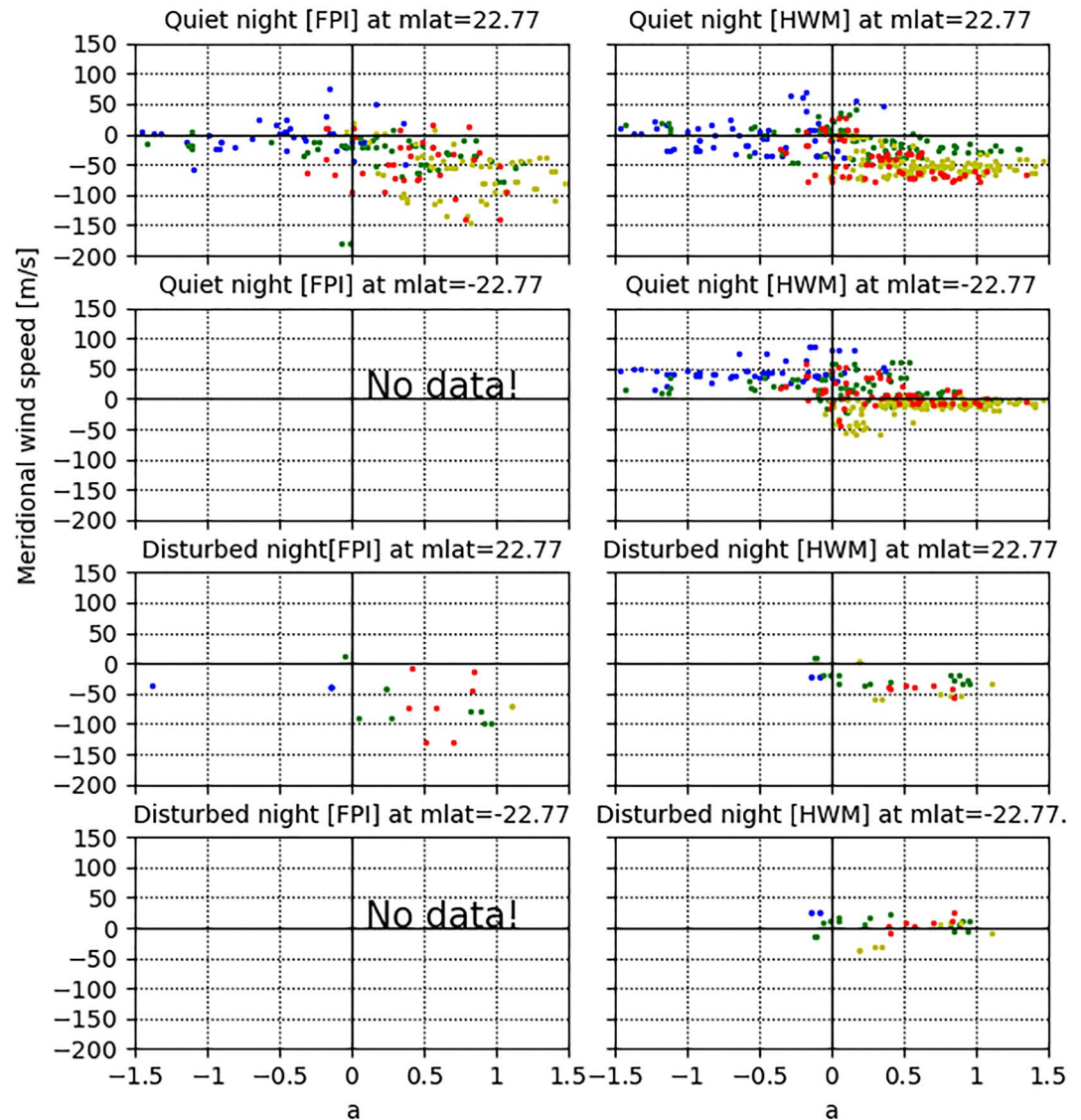


**Figure 9.** Fabry–Perot interferometer (FPI) meridional wind speed averaged over an hour before the overpass of the Swarm satellites (right side of the plot) as a function of the index ( $a$ ) over 3 years of all SWA, SWB, and SWC overflight during quiet (two top set of plots) and disturbed (two bottom set of plots) nights. Horizontal Wind Model (HWM) model predictions (left set of plots) at the magnetic latitude of Oukaimeden ( $+22.77^\circ\text{N}$ ) and at its conjugate latitude ( $-22.77^\circ\text{N}$ ) latitude are illustrated. The data are sorted by season: around December solstice (blue points), March equinox (green points), June solstice (yellow points), and September equinox (red points). Positive values are poleward for meridional winds in both hemispheres.

### 3.3.2. Quantifying the Effect of Meridional Winds on the EIA Asymmetry

Figure 9 shows the FPI meridional wind speed averaged over an hour before the overpass of the Swarm satellites (right side of the plot) as a function of the index ( $a$ ) over 3 years. All SWA, SWB, and SWC overflights during quiet (two top sets of plots) and disturbed (two bottom sets of plots) nights are shown. HWM model predictions (left set of plots) at the magnetic latitude of Oukaimeden ( $+22.77^\circ\text{N}$ ) and at its conjugate latitude ( $-22.77^\circ\text{N}$ ) latitude are illustrated. The data are sorted by season: around December solstice (blue points), March equinox (green points), June solstice (yellow points), and September equinox (red points). Positive values are poleward for meridional winds in both hemispheres.

From FPI data over Oukaimeden (left top panel), it is evident that EIA crest asymmetry is the most probable phenomena with the northern crest higher than the southern one ( $a \geq 0$ ) along with equatorward winds ( $V \leq 0$ ). Indeed from FPI wind data climatology (Kaab et al., 2017; Loufi et al., 2020), equatorward winds are most

probable during the course of the night especially during September and March equinoxes and June solstice. The December solstice data (blue dots) are characterized with a negative asymmetry index  $a \leq 0$  (the southern crest higher than the northern one) and low wind speed. We can notice that HWM predictions over Oukaimeden Observatory resemble the FPI data however with lower values for the June solstice.

HWM data predictions at the Oukaimeden Observatory conjugate site are provided to look for the convergent (equatorward wind in both hemispheres) or divergent (poleward wind in both hemispheres or transequatorial [northward or southward]) nature of meridional winds over the studied area. For December solstice, from HWM predictions we conclude the existence of two types of regimes: transequatorial winds directed to the South and divergent winds. For June solstice, transequatorial winds directed to the South prevail with also a small occurrence of convergent winds. Southward transequatorial winds also prevail during the September and March equinoxes.

This effect of the meridional wind on asymmetry generation can be explained by the plasma recombination as already explained in Section 1. In the case of geomagnetic storms, the EIA asymmetry is pronounced in the Northern Hemisphere because of the equatorward component of the disturbed winds due to sudden storm energy deposition. HWM predicts Southward transequatorial winds for most of the geomagnetic storms. We can notice that the asymmetry index is positive ( $a \geq 0$ ) for most of the storms except for the December solstice. Balan et al. (2018) gave two hypothesis concerning quiet time equatorial plasma fountain mechanisms; (a) at all altitudes, perpendicular  $E \times B$  plasma drift and field-aligned plasma diffusion work together along the field lines, leading plasma to flow in the resultant's direction, (b) the EIA is formed not from the accumulation of plasma at the crests but mainly from the removal of plasma from around the magnetic equator by the upward  $E \times B$  drift with small accumulations when the crests are within approximately  $\sim \pm 20^\circ$  magnetic latitude. The accumulations reduce with increasing latitude and become zero around  $\sim \pm 25^\circ$ . They also reported that under disturbed conditions the EIA becomes strong due to the combined impulsive action of both eastward prompt penetration electric field (PPEF) and storm time equatorward winds (SEW). SEW (with normal electric field) alone can produce strong EIA while PPEF alone is unlikely. Khadka et al. (2018) explained the effects of the meridional winds on EIA asymmetry generation by two ways: (a) intrahemispheric transport and (b) transequatorial transport. In the case of (a) intrahemispheric transport, the meridional neutral wind is blowing north to south (south to north), it will drive plasma to higher ionospheric heights along field lines where recombination proceeds at a slower rate. This leads to higher plasma density in the Northern (Southern) Hemisphere. In the case of (b) transequatorial transport, the meridional neutral wind is blowing north to south (south to north), it will transport plasma along Earth's magnetic field lines and will dump at ionospheric height in the opposite hemisphere since the effect of a weak equatorial plasma fountain is easily overcome by the wind. That leads to a higher plasma density in the Southern (Northern) Hemisphere than that in northern (southern) crests. However, Amaechi et al. (2020) reported the same scenario to explain the effects of the meridional winds on EIA asymmetry generation adding that to the third case of the EIA symmetry due to no wind effect or equal wind strengths from both hemispheres. The numerical work by Abur-Robb and Windle (1969) also showed similar characteristics, and they proposed that plasma transport by neutral winds from the summer hemisphere to the winter hemisphere is the dominant factor that leads to the daytime asymmetries, whereas molecular recombination dominates at night and the peak height is much lower in the winter hemisphere than in the summer hemisphere, leading to the nighttime asymmetries. By using the physics-based National Center for Atmospheric Research Thermosphere–Ionosphere Electrodynamics Global Circulation Model (Dang et al., 2016), compared the role of meridional neutral winds, photochemical effects, and magnetic field configuration played in the EIA interhemispheric asymmetry. They reported that the transequatorial neutral wind is the major contributor to the north-south asymmetry.

#### 4. Conclusions

This paper's main focus was to explore the effect of thermospheric winds on the EIA crest asymmetry during both quiet and disturbed conditions. For that purpose, Swarm density data of a magnetic meridian line over Oukaimeden Observatory along with FPI wind data of the same observatory (3 years of measurements, from 2014 to 2016) have been used to achieve this study. A thorough study of the annual and seasonal behavior of the ionospheric density provided by Swarm satellites has been achieved first to establish the variations modalities of the

ionospheric density over this meridional line. Then, a correlation is established between the EIA crest asymmetry/symmetry and the meridional winds regime. From our work, we have drawn the following main conclusions:

1. The annual variation of the electron density in low- and midlatitude topside ionosphere at different local time sectors shows lower electron densities during nighttime than daytime. During the day, the ionospheric density starts to increase at midlatitudes, with a single crest between 8 LT and 12 LT. The double crest structure is present between 12 LT and midnight: symmetric from noon to 20 LT and asymmetric from 20 LT to 24 LT.
2. Observations show strong seasonal variations, with the electron density being lower around the June solstice compared to the rest of the year. We have noticed the semiannual anomaly: the electron density is higher around equinoxes than around solstices. For solstice seasons, the asymmetries in the electron density are stronger at the December solstice than at the June one. During the June solstice, the EIA northern crest is higher than the southern one ( $a \geq 0$ ) and the opposite is observed during the December solstice. For equinox seasons, we can notice equinoctial symmetry in all local time sectors, meaning that the same trend is observed for both equinoxes with or without symmetrical crests.
3. We have also observed a hemispheric asymmetry in the evolution of the electron density where it decreases slowly with latitude in the Southern Hemisphere whereas the opposite is observed in the northern one. This asymmetry could find its origin in the asymmetry of the magnetic field itself.
4. When comparing the EIA crests and the meridional winds regime, two types of responses have been noticed for both quiet and disturbed conditions. The symmetrical EIA crests are most likely due to weak wind speeds or to converging/diverging winds with about the same velocity in both hemispheres. Concerning the second type, a northward or southward transequatorial meridional wind is a good candidate for this EIA asymmetry generation.
5. During disturbed geomagnetic conditions, almost all of them give rise to a northern EIA crest higher than the southern one, related in general to transequatorial meridional winds regime.

### Appendix A: The Average and Seasonal Variations of the Ionospheric Density Peaks

In this paragraph, Tables A1, A2, A3, A4 and A5 present more information about the density at the peak and its magnetic latitude and the number of satellite passes taken the analysis.

**Table A1**

*The Values of the Ionospheric Density Peaks (Single or Double) Along With Their Magnetic Latitude and That of the Through for SWA (Figure 5)*

Season-Sat	Sector [LT]	$N_e$ (NC) ( $10^5 \text{ cm}^{-3}$ )	Mlat (NC) ( $^\circ$ )	$N_e$ (SC) ( $10^5 \text{ cm}^{-3}$ )	Mlat (SC) ( $^\circ$ )	$N_e$ (trough) ( $10^5 \text{ cm}^{-3}$ )	Mlat (trough) ( $^\circ$ )	Index $a$
Mar-A	[0:4]	3.66	14	2.12	-11	1.79	-6	0.53
Mar-A	[8:12]	5.59	0	5.59	0	-	-	-
Mar-A	[12:16]	14.19	10	14.03	-13	10.37	-3	0.01
Mar-A	[16:20]	11.38	9	10.58	-14	8.4	-3	0.07
Mar-A	[20:24]	9.5	10	6.27	-15	3.86	-4	0.41
Jun-A	[0:4]	2.65	23	0.87	-10	0.65	-4	1.01
Jun-A	[8:12]	-	-	5.22	-1	-	-	-
Jun-A	[12:16]	7.42	9	6.01	-10	5.37	-3	0.21
Jun-A	[16:20]	5.57	6	-	-	-	-	0.05
Jun-A	[20:24]	4.32	15	2.36	-8	1.82	-1	0.59
Spt-A	[0:4]	1.71	12	1.27	0	1.06	-7	0.29
Spt-A	[8:12]	8.18	5	8.22	-10	-	-	-0.0
Spt-A	[12:16]	9.53	9	9.66	-13	7.27	-2	-0.01
Spt-A	[16:20]	8.21	10	8.31	-11	6.78	3	-0.01
Spt-A	[20:24]	7.16	9	6.41	-13	4.25	-3	0.11
Dec-A	[0:4]	-	-	1.99	-13	-	-	-0.22

**Table A1**  
*Continued*

Season-Sat	Sector [LT]	$N_e$ (NC) ( $10^5 \text{ cm}^{-3}$ )	Mlat (NC) ( $^\circ$ )	$N_e$ (SC) ( $10^5 \text{ cm}^{-3}$ )	Mlat (SC) ( $^\circ$ )	$N_e$ (trough) ( $10^5 \text{ cm}^{-3}$ )	Mlat (trough) ( $^\circ$ )	Index $a$
Dec-A	[8:12]	–	–	6.28	–10	–	–	–
Dec-A	[12:16]	7.93	10	10.87	–15	6.78	–2	–0.31
Dec-A	[16:20]	10.73	11	11.73	–17	6.04	–2	–0.09
Dec-A	[20:24]	4.16	7	4.91	–16	2.64	–5	–0.17

*Note.* These parameters have been determined for the electron density of EIA crest in the Northern Hemisphere. We selected the maximum value of electron density between  $5^\circ$  and  $30^\circ$  and between their corresponding magnetic latitudes. Using the same method, we determined EIA crest in the Southern Hemisphere. For the electron density of the trough, we selected the minimum value of electron density in the range  $\mp 10$  and between their corresponding magnetic latitude.

**Table A2**  
*Same as Table A1, But for SWB (Figure 7)*

Season-Sat	Sector [LT]	$N_e$ (NC) ( $10^5 \text{ cm}^{-3}$ )	Mlat (NC) ( $^\circ$ )	$N_e$ (SC) ( $10^5 \text{ cm}^{-3}$ )	Mlat (SC) ( $^\circ$ )	$N_e$ (trough) ( $10^5 \text{ cm}^{-3}$ )	Mlat (trough) ( $^\circ$ )	Index $a$
Mar-B	[0:4]	2.26	11.0	–	–	–	–	–
Mar-B	[8:12]	–	–	3.89	–2.0	–	–	–
Mar-B	[12:16]	12.85	8	12.67	–11	10.7	–2	0.01
Mar-B	[16:20]	15.51	9	15.17	–13	12.18	–3	0.02
Mar-B	[20:24]	4.19	8	2.76	–5	2.22	0	0.41
Jun-B	[0:4]	1.87	19	0.71	–10	0.57	0	0.9
Jun-B	[8:12]	3.13	0	–	–	–	–	–
Jun-B	[12:16]	3.63	4	–	–	–	–	–
Jun-B	[16:20]	4.17	5	–	–	–	–	–
Jun-B	[20:24]	4.54	11	3.2	–7	2.23	–1	0.34
Spt-B	[0:4]	1.72	13	1.2	–10	1.14	–7	0.36
Spt-B	[8:12]	–	–	5.3	–3.0	–	–	–
Spt-B	[12:16]	–	–	6.97	–9	–	–	–
Spt-B	[16:20]	–	–	5.17	–8	–	–	–
Spt-B	[20:24]	4.99	8	4.01	–13	3.68	–2	0.22
Dec-B	[0:4]	1.46	7	1.61	–11	1.26	–2	–0.1
Dec-B	[8:12]	–	–	5.07	–8	–	–	–
Dec-B	[12:16]	9.44	10	11.86	–15	7.88	–2	–0.23
Dec-B	[16:20]	8.38	9	10.02	–16	5.61	–3	–0.18
Dec-B	[20:24]	4.37	6	5.16	–17	2.63	–3	–0.17

**Table A3**

Same as Table A1, But for SWC (Figure 6)

Season -Sat	Sector [LT]	$N_e$ (NC) ( $10^5\text{cm}^{-3}$ )	Mlat (NC) ( $^\circ$ )	$N_e$ (SC) ( $10^5\text{cm}^{-3}$ )	Mlat (SC) ( $^\circ$ )	$N_e$ (trough) ( $10^5\text{cm}^{-3}$ )	Mlat (trough) ( $^\circ$ )	Index <i>a</i>
Mar-C	[0:4]	3.65	13	2.09	-12	1.63	-4	0.55
Mar-C	[8:12]	-	-	5.92	0	-	-	-
Mar-C	[12:16]	13.2	9	13.22	-13	10.05	-3	-0.0
Mar-C	[16:20]	11.51	8	10.78	-12	9.6	-5	0.07
Mar-C	[20:24]	7.49	10	4.83	-12	3.4	-5	0.43
Jun-C	[0:4]	2.7	25	0.85	-10	0.69	-5	1.04
Jun-C	[8:12]	-	-	5.2	-1	-	-	-
Jun-C	[12:16]	7.2	10	5.65	-9	5.33	-3	0.24
Jun-C	[16:20]	6.44	9	-	-	-	-	-
Jun-C	[20:24]	4.9	19	2.79	-7	2.19	-2	0.55
Spt-C	[0:4]	1.66	10	-	-	-	-	-
Spt-C	[8:12]	8.32	2	-	-	-	-	-
Spt-C	[12:16]	9.41	11	9.71	-14	7.03	-2	-0.03
Spt-C	[16:20]	7.07	7	7.25	-9	6.15	4	-0.02
Spt-C	[20:24]	8.15	9	5.79	-14	4.07	-8	0.34
Dec-C	[0:4]	-	-	1.86	-11	-	-	-
Dec-C	[8:12]	5.84	2.0	-	-	-	-	-
Dec-C	[12:16]	8.35	9	10.41	-15	7.3	-3	-0.22
Dec-C	[16:20]	13.85	12	13.84	-17	5.51	-3	0.0
Dec-C	[20:24]	3.97	9	4.91	-16	2.58	-3	-0.21

**Table A4**

The Number of Satellite Passes Taken for the Analysis for Annual Variability of Ionosphere Electron Density (Figure 3)

Satellite	Sector LT	Number
A	[0:4]	82
A	[4:8]	76
A	[8:12]	69
A	[12:16]	34
A	[16:20]	41
A	[20:24]	39
B	[0:4]	84
B	[4:8]	76
B	[8:12]	67
B	[12:16]	16
B	[16:20]	17
B	[20:24]	32
C	[0:4]	77
C	[4:8]	81
C	[8:12]	66
C	[12:16]	41
C	[16:20]	40
C	[20:24]	36

**Table A5**  
The Number of Satellite Passes Taken for the Analysis for Seasonal Variability of Ionosphere Electron Density (Figures 5–7)

Satellite	Sector LT	Number	Satellite	Sector LT	Number	Satellite	Sector LT	Number
Mar-A	[0:4]	23	Mar-B	[0:4]	28	Mar-C	[0:4]	19
Mar-A	[4:8]	29	Mar-B	[4:8]	28	Mar-C	[4:8]	31
Mar-A	[8:12]	20	Mar-B	[8:12]	19	Mar-C	[8:12]	19
Mar-A	[12:16]	13	Mar-B	[12:16]	5	Mar-C	[12:16]	13
Mar-A	[16:20]	16	Mar-B	[16:20]	6	Mar-C	[16:20]	17
Mar-A	[20:24]	8	Mar-B	[20:24]	11	Mar-C	[20:24]	11
Jun-A	[0:4]	24	Jun-B	[0:4]	26	Jun-C	[0:4]	24
Jun-A	[4:8]	24	Jun-B	[4:8]	25	Jun-C	[4:8]	27
Jun-A	[8:12]	27	Jun-B	[8:12]	28	Jun-C	[8:12]	28
Jun-A	[12:16]	8	Jun-B	[12:16]	4	Jun-C	[12:16]	13
Jun-A	[16:20]	11	Jun-B	[16:20]	7	Jun-C	[16:20]	10
Jun-A	[20:24]	20	Jun-B	[20:24]	9	Jun-C	[20:24]	16
Spt-A	[0:4]	35	Spt-B	[0:4]	30	Spt-C	[0:4]	34
Spt-A	[4:8]	23	Spt-B	[4:8]	23	Spt-C	[4:8]	23
Spt-A	[8:12]	22	Spt-B	[8:12]	20	Spt-C	[8:12]	19
Spt-A	[12:16]	13	Spt-B	[12:16]	7	Spt-C	[12:16]	15
Spt-A	[16:20]	14	Spt-B	[16:20]	4	Spt-C	[16:20]	13
Spt-A	[20:24]	11	Spt-B	[20:24]	12	Spt-C	[20:24]	9

## Data Availability Statement

The LOS wind data used in this study are freely available for use in the Madrigal database <http://madrigal.haystack.mit.edu/madrigal/>. Please contact Jonathan J. Makela ([jmakela@illinois.edu](mailto:jmakela@illinois.edu)) before using these data. The SYM-H index storm can be downloaded from <https://omniweb.gsfc.nasa.gov/>. The International Service of Geomagnetic Indices (ISGI) is in charge of the elaboration and dissemination of geomagnetic indices (Kp; from <http://isgi.unistra.fr>). We thank Douglas Drob for providing the HWM14 code and Timothy Duly for developing a Python wrapper for that model (Pyglow), available at <https://github.com/timduly4/pyglow/>. The European Space Agency is acknowledged for providing the Swarm data. The official Swarm website is <https://swarm-diss.esa.int/>.

## Acknowledgments

This project is financially supported by Campus France through the French–Moroccan bilateral program “PHC Toubkal 2019” (grant number: 41409WJ).

## References

- Abur-Robb, M., & Windle, D. (1969). On the day and night reversal in NmF2 North-South asymmetry. *Planetary and Space Science*, 17(1), 97–106. [https://doi.org/10.1016/0032-0633\(69\)90126-3](https://doi.org/10.1016/0032-0633(69)90126-3)
- Amaechi, P. O., Oyeyemi, E. O., Akala, A. O., & Amory Mazaudier, C. (2020). Geomagnetic activity control of irregularities occurrences over the crests of the African EIA. *Earth and Space Science*, 7, e2020EA001183. <https://doi.org/10.1029/2020EA001183>
- Anderson, D. N. (1973). A theoretical study of ionospheric F region equatorial anomaly—I. Theory. *Planetary and Space Science*, 21, 409–419. [https://doi.org/10.1016/0032-0633\(73\)90040-8](https://doi.org/10.1016/0032-0633(73)90040-8)
- Appleton, E. V. (1946). Two anomalies in the ionosphere. *Nature*, 157(3995), 691. <https://doi.org/10.1038/157691a0>
- Bailey, G. J., & Balan, N. (1996). Some modelling studies of the equatorial ionosphere using the Sheffield University plasmasphere ionosphere model. *Advances in Space Research*, 18(6), 59–68. [https://doi.org/10.1016/0273-1177\(95\)00901-9](https://doi.org/10.1016/0273-1177(95)00901-9)
- Bailey, G. J., Su, Y. Z., & Oyama, K.-I. (2000). Yearly variations in the low-latitude topside ionosphere. *Annales Geophysicae*, 18(7), 789–798. <https://doi.org/10.1007/s00585-000-0789-0>
- Balan, N., & Bailey, G. J. (1995). Equatorial plasma fountain and its effects: Possibility of an additional layer. *Journal of Geophysical Research*, 100(A11), 21421–21432. <https://doi.org/10.1029/95JA01555>
- Balan, N., Liu, L., & Le, H. (2018). A brief review of equatorial ionization anomaly and ionospheric irregularities. *Earth and Planetary Physics*, 2(4), 1–19. <https://doi.org/10.26464/epp2018025>
- Balan, N., Rajesh, P. K., Sripathi, S., Tulasiram, S., Liu, J. Y., & Bailey, G. J. (2013). Modeling and observations of the north–south ionospheric asymmetry at low latitudes at long deep solar minimum. *Advances in Space Research*, 52(3), 375–382. <https://doi.org/10.1016/j.asr.2013.04.003>

- Barlier, F., Bauer, P., Jaeck, C., Thuillier, G., & Kockarts, G. (1974). North-south asymmetries in the thermosphere during the last maximum of the solar cycle. *Journal of Geophysical Research*, 79(34), 5273–5285. <https://doi.org/10.1029/JA079i034p05273>
- Bittencourt, J. A., Pillat, V. G., Fagundes, P. R., Sahai, Y., & Pimenta, A. A. (2007). LION: A dynamic computer model for the low-latitude ionosphere. *Annales Geophysicae*, 25(11), 2371–2392. <https://doi.org/10.5194/angeo-25-2371-2007>
- Bolaji, O., Owolabi, O., Falayi, E., Jimoh, E., Kotoye, A., Odeyemi, O., et al. (2017). Observations of equatorial ionization anomaly over Africa and Middle East during a year of deep minimum. *Annales Geophysicae*, 35, 123–132. <https://doi.org/10.5194/angeo-35-123-2017>
- Bosco, O., Edward, J., & Nicolausi, S. (2016). Variations of crest-to-trough TEC ratio of the East African equatorial anomaly region. *International Journal of Astrophysics and Space Science*, 4(1), 12–20. <https://doi.org/10.11648/j.ijass.20160401.12>
- Chen, Y., Liu, L., Le, H., Wan, W., & Zhang, H. (2017). The effect of zonal wind dynamic reversal around sunset on ionospheric interhemispheric asymmetry at march equinox of a solar maximum year 2000. *Journal of Geophysical Research: Space Physics*, 122, 4726–4735. <https://doi.org/10.1002/2017JA023874>
- Dang, T., Luan, X., Lei, J., Dou, X., & Wan, W. (2016). A numerical study of the interhemispheric asymmetry of the equatorial ionization anomaly in solstice at solar minimum. *Journal of Geophysical Research: Space Physics*, 121, 9099–9110. <https://doi.org/10.1002/2016JA023012>
- Davies, K. (1990). *Ionospheric radio*. Peter Peregrinus Ltd.
- Drob, D. P., Emmert, J. T., Meriwether, J. W., Makela, J. J., Doornbos, E., Conde, M., et al. (2015). An update to the Horizontal Wind Model (HWM): The quiet time thermosphere. *Earth and Space Science*, 2, 301–319. <https://doi.org/10.1002/2014EA000089>
- Emmert, J., Picone, J. M., & Meier, R. R. (2008). Thermospheric global average density trends, 1967–2007, derived from orbits of 5000 near-Earth objects. *Geophysical Research Letters*, 35, L05101. <https://doi.org/10.1029/2007GL032809>
- Emmert, J., Richmond, A., & Drob, D. (2010). A computationally compact representation of magnetic-apex and quasi-dipole coordinates with smooth base vectors. *Journal of Geophysical Research*, 115, A08322. <https://doi.org/10.1029/2010JA015326>
- Fathy, A., & Ghamry, E. (2017). A statistical study of single crest phenomenon in the equatorial ionospheric anomaly region using Swarm A satellite. *Advances in Space Research*, 59(6), 1539–1547. <https://doi.org/10.1016/j.asr.2016.12.020>
- Fejer, B. G., Jensen, J. W., & Su, S.-Y. (2008). Seasonal and longitudinal dependence of equatorial disturbance vertical plasma drifts. *Geophysical Research Letters*, 35, L20106. <https://doi.org/10.1029/2008GL035584>
- Fisher, D. J., Makela, J. J., Meriwether, J. W., Burity, R. A., Benkhaldoun, Z., Kaab, M., & Lagheryeb, A. (2015). Climatologies of nighttime thermospheric winds and temperatures from Fabry–Perot interferometer measurements: From solar minimum to solar maximum. *Journal of Geophysical Research: Space Physics*, 120, 6679–6693. <https://doi.org/10.1002/2015JA021170>
- Forster, M., & Cnossen, I. (2013). Upper atmosphere differences between northern and southern high latitudes: The role of magnetic field asymmetry. *Journal of Geophysical Research: Space Physics*, 118, 5951–5966. <https://doi.org/10.1002/jgra.50554>
- Friis-Christensen, E., Luhr, H., Knudsen, D., & Haagmans, R. (2008). Swarm—An Earth observation mission investigating geospace. *Advances in Space Research*, 41(1), 210–216. <https://doi.org/10.1016/j.asr.2006.10.008>
- Fuller-Rowell, T. J. (1998). The “thermospheric spoon”: A mechanism for the semiannual density variation. *Journal of Geophysical Research*, 103(A3), 3951–3956. <https://doi.org/10.1029/97JA03335>
- Hanson, W. B., & Moffett, R. J. (1966). Ionization transport effects in the equatorial F region. *Journal of Geophysical Research*, 71(23), 5559–5572. <https://doi.org/10.1029/JZ071i023p05559>
- Harding, B. J., Gehrels, T. W., & Makela, J. J. (2014). Nonlinear regression method for estimating neutral wind and temperature from Fabry–Perot interferometer data. *Applied Optics*, 53, 666–673. <https://doi.org/10.1364/AO.53.000666>
- Immel, T. J., England, S. L., Mende, S. B., Heelis, R. A., Englert, C. R., Edelstein, J., et al. (2018). The ionospheric connection explorer mission: Mission goals and design. *Space Science Reviews*, 214(1), 13. <https://doi.org/10.1007/s11214-017-0449-2>
- Kaab, M., Benkhaldoun, Z., Fisher, D. J., Harding, B., Bounhir, A., Makela, J. J., et al. (2017). Climatology of thermospheric neutral winds over Oukaimeden Observatory in Morocco. *Annales Geophysicae*, 35(1), 161–170. <https://doi.org/10.5194/angeo-35-161-2017>
- Kalita, B., Bhuyan, P., Nath, S., Choudhury, M., Chakrabarty, D., Wang, K., et al. (2022). The investigation on daytime conjugate hemispheric asymmetry along 100°E longitude using observations and model simulations: New insights. *Advances in Space Research*, 69(10), 3726–3740. <https://doi.org/10.1016/j.asr.2022.02.058>
- Kassa, T., Damtie, B., Bires, A., Yizengaw, E., & Cilliers, P. (2014). Spatio-temporal characteristics of the equatorial ionization anomaly (EIA) in the East African region via ionospheric tomography during the year 2012. *Advances in Space Research*, 55, 184–198. <https://doi.org/10.1016/j.asr.2014.09.001>
- Kelley, M. (2009). *The Earth's ionosphere. International geophysics (Book 96)* (2nd ed.). Academic Press.
- Khadka, S. M., Valladares, C. E., Sheehan, R., & Gerrard, A. J. (2018). Effects of electric field and neutral wind on the asymmetry of equatorial ionization anomaly. *Radio Science*, 53, 683–697. <https://doi.org/10.1029/2017RS006428>
- Laundal, K. M., Cnossen, I., Milan, S. E., Haaland, S. E., Coxon, J., Pedatella, N. M., et al. (2017). North–South asymmetries in Earth's magnetic field. *Space Science Reviews*, 206(1–4), 225–257. <https://doi.org/10.1007/s11214-016-0273-0>
- Lin, C. H., Liu, J. Y., Fang, T. W., Chang, P. Y., Tsai, H. F., Chen, C. H., & Hsiao, C. C. (2007). Motions of the equatorial ionization anomaly crests imaged by FORMOSAT-3/COSMIC. *Geophysical Research Letters*, 34, L19101. <https://doi.org/10.1029/2007GL030741>
- Loutfi, A., Bounhir, A., Pitout, F., Benkhaldoun, Z., & Makela, J. J. (2020). Thermospheric neutral winds above the Oukaimeden Observatory: Effects of geomagnetic activity. *Journal of Geophysical Research: Space Physics*, 125, e2019JA027383. <https://doi.org/10.1029/2019JA027383>
- Luan, X., Wang, P., Dou, X., & Liu, Y. C.-M. (2015). Interhemispheric asymmetry of the equatorial ionization anomaly in solstices observed by cosmic during 2007–2012. *Journal of Geophysical Research: Space Physics*, 120, 3059–3073. <https://doi.org/10.1002/2014JA020820>
- Makela, J. J., Meriwether, J. W., Huang, Y., & Sherwood, P. J. (2011). Simulation and analysis of a multi-order imaging Fabry–Perot interferometer for the study of thermospheric winds and temperatures. *Applied Optics*, 50, 4403–4416. <https://doi.org/10.1364/AO.50.004403>
- Makela, J. J., Meriwether, J. W., Lima, J. P., Miller, E. S., & Armstrong, S. J. (2009). The Remote Equatorial Nighttime Observatory of Ionospheric Regions project and the International Heliospherical Year. *Earth, Moon, and Planets*, 104, 211–226. <https://doi.org/10.1007/s11038-008-9289-0>
- Malki, K., Bounhir, A., Benkhaldoun, Z., Makela, J. J., Vilmer, N., Fisher, D. J., et al. (2018). Ionospheric and thermospheric response to the 27–28 February 2014 geomagnetic storm over North Africa. *Annales Geophysicae*, 36(4), 987–998. <https://doi.org/10.5194/angeo-36-987-2018>
- Martyn, D. F. (1947). Atmospheric tides in the ionosphere. 1. Solar tides in the F2 region. *Proceedings of the Royal Society of London A*, 189(1017), 241–260. <https://doi.org/10.1098/rspa.1947.0037>
- Millward, G. H., Moffett, R. J., Quegan, S., & Fuller-Rowell, T. J. (1996). A Coupled Thermosphere–Ionosphere–Plasmasphere model (CTIP). In R. W. Schunk (Ed.), *STEP handbook on ionospheric models* (pp. 239–279). Utah State University.
- MITRA, S. (1946). Geomagnetic control of region F2 of the ionosphere. *Nature*, 158, 668–669. <https://doi.org/10.1038/158668a0>

- Oliveira, C., Espejo, T., Moraes, A., Costa, E., Sousasantos, J., Lourenço, L. F. D., & Abdu, M. A. (2020). Analysis of plasma bubble signatures in total electron content maps of the low-latitude ionosphere: A simplified methodology. *Surveys in Geophysics*, *41*, 897–931. <https://doi.org/10.1007/s10712-020-09584-7>
- Rishbeth, H., & Setty, C. S. G. K. (1961). The *F*-layer at sunrise. *Journal of Atmospheric and Terrestrial Physics*, *20*(4), 263–276. [https://doi.org/10.1016/0021-9169\(61\)90205-7](https://doi.org/10.1016/0021-9169(61)90205-7)
- Rüster, R., & King, J. (1973). Atmospheric composition changes and the *F2*-layer seasonal anomaly. *Journal of Atmospheric and Terrestrial Physics*, *35*, 1317–1322. [https://doi.org/10.1016/0021-9169\(73\)90164-5](https://doi.org/10.1016/0021-9169(73)90164-5)
- Sastri, J. H. (1990). Equatorial anomaly in *F*-region—A review. *Indian Journal of Radio and Space Physics*, *19*(4), 225–240.
- Schunk, R. W., & Nagy, A. F. (2000). *Ionosphere: Physics, plasma and chemistry*. Cambridge University Press. <https://doi.org/10.1017/CBO9780511551772>
- Su, Y., Bailey, G., & Oyama, K. (1998). Annual and seasonal variations in the low-latitude topside ionosphere. *Annales Geophysicae*, *16*, 974–985. <https://doi.org/10.1007/s00585-998-0974-0>
- Thébault, E., Finlay, C., Beggan, C., Alken, P., Aubert, J., Barrois, O., et al. (2015). International Geomagnetic Reference Field: The 12th generation. *Earth, Planets and Space*, *67*, 79. <https://doi.org/10.1186/s40623-015-0228-9>
- Titheridge, J. E., & Buonsanto, M. J. (1983). Annual variations in the electron content and height of the *F* layer in the Northern and Southern Hemispheres, related to neutral composition. *Journal of Atmospheric and Terrestrial Physics*, *45*(10), 683–696. [https://doi.org/10.1016/S0021-9169\(83\)80027-0](https://doi.org/10.1016/S0021-9169(83)80027-0)
- Tulasi Ram, S., Su, S.-Y., & Liu, C. H. (2009). FORMOSAT-3/COSMIC observations of seasonal and longitudinal variations of equatorial ionization anomaly and its interhemispheric asymmetry during the solar minimum period. *Journal of Geophysical Research*, *114*, A06311. <https://doi.org/10.1029/2008JA013880>
- Wan, X., Zhong, J., Xiong, C., Wang, H., Liu, Y., Li, Q., et al. (2022). Seasonal and interhemispheric effects on the diurnal evolution of EIA: Assessed by IGS TEC and IRI-2016 over Peruvian and Indian sectors. *Remote Sensing*, *14*(1), 107. <https://doi.org/10.3390/rs14010107>
- Wu, C.-C., Fry, C. D., Liu, J. Y., Liou, K., & Tseng, C. L. (2004). Annual TEC variation in the equatorial anomaly region during the solar minimum: September 1996–August 1997. *Journal of Atmospheric and Solar-Terrestrial Physics*, *66*(3–4), 199–207. <https://doi.org/10.1016/j.jastp.2003.09.017>
- Wu, C.-C., Liou, K., Shan, S.-J., & Tseng, C.-L. (2008). Variation of ionospheric total electron content in Taiwan region of the equatorial anomaly from 1994 to 2003. *Advances in Space Research*, *41*(4), 611–616. <https://doi.org/10.1016/j.asr.2007.06.013>
- Xiong, C., & Lüher, H. (2013). Nonmigrating tidal signatures in the magnitude and the inter-hemispheric asymmetry of the equatorial ionization anomaly. *Annales Geophysicae*, *31*(6), 1115–1130. <https://doi.org/10.5194/angeo-31-1115-2013>
- Xiong, C., Luhr, H., & Ma, S. Y. (2013). The magnitude and inter-hemispheric asymmetry of equatorial ionization anomaly-based on champ and grace observations. *Journal of Atmospheric and Solar-Terrestrial Physics*, *105–106*, 160–169. <https://doi.org/10.1016/j.jastp.2013.09.010>
- Yonezawa, T. (1971). The solar-activity and latitudinal characteristics of the seasonal, non-seasonal and semi-annual variations in the peak electron densities of the *F2*-layer at noon and at midnight in middle and low latitudes. *Journal of Atmospheric and Terrestrial Physics*, *33*, 889–907. [https://doi.org/10.1016/0021-9169\(71\)90089-4](https://doi.org/10.1016/0021-9169(71)90089-4)